Soft Matter

PAPER

View Article Online
View Journal

Cite this: DOI: 10.1039/d3sm01474f

Optimal face-to-face coupling for fast self-folding kirigami†

Maks Pecnik Bambic, [abc] Nuno A. M. Araújo, [de] Benjamin J. Walker, [fg] Duncan R. Hewitt, [gh] Qing Xiang Pei, [b] Ran Ni [c] and Giorgio Volpe *[a]

Received 1st November 2023,
Accepted 8th January 2024

DOI: 10.1039/d3sm01474f

rsc.li/soft-matter-journal

Kirigami-inspired designs can enable self-folding three-dimensional materials from flat, two-dimensional sheets. Hierarchical designs of connected levels increase the diversity of possible target structures, yet they can lead to longer folding times in the presence of fluctuations. Here, we study the effect of rotational coupling between levels on the self-folding of two-level kirigami designs driven by thermal noise in a fluid. Naturally present due to hydrodynamic resistance, we find that this coupling parameter can significantly impact a structure's self-folding pathway, thus enabling us to assess the quality of a kirigami design and the possibility for its optimization in terms of its folding rate and yield.

Introduction

The art of kirigami, where three-dimensional shapes emerge from flat sheets (templates) through prescribed cuts and folds, is pursued as a route to design programmable materials that can self-fold into target structures across scales.[1–3] Kirigami-inspired designs are promising due to the easiness of two-dimensional fabrication and for their potential for deployability and reconfigurability.[1–3] Applications include morphable structures and sheets,[4–8] mechanical actuators,[9,10] nanocomposites,[11,12] metamaterials[13–15] and soft robots.[16–20]

Due to the broad interest in kirigami designs, the quest to understand the geometrical, topological and mechanical principles behind their folding dynamics has driven a large body of research,[21–24] which has also sought to define design rules to optimize them.[25–28] At macroscopic scales, as folding is usually driven by stress relaxation,[27–29] deterministic rules can be identified and relied upon directly.[28,30–32] However, at microscopic scales, thermal noise can render the folding dynamics a stochastic process.[33–38]

Thermal fluctuations are critical to how microscopic systems explore their configuration space and converge to the desired target structures.[25,36–38] Due to these fluctuations, the folding trajectories are stochastic and the final configuration might not coincide with the desired one. The trajectories depend on the initial template's choice,[25] the materials properties,[21] and the experimental conditions.[36] Nonetheless, in some systems, if an undesired configuration is reached, the thermal energy provided by the surroundings might not be sufficient to reverse binding events, rendering them effectively irreversible, *e.g.* when liquid metal hinges fuse after folding driven by surface tension minimization[25] or in DNA origami, where structures cannot come undone below the melting temperature of DNA.[39] Folding yield (the proportion of templates that successfully fold into the target structure within a given time) has therefore been an important parameter to optimize.[22,25] Beyond yield, folding time is an equally key parameter for real-life applications of microscopic kirigami designs, yet its optimization is much less understood. An accurate prediction of the folding time was possible for simple single level structures.[37,38] However, kirigami designs often present multiple interdependent levels, whose folding could strongly depend on level-to-level correlations, *e.g.* due to materials or environmental properties.[34,35,40,41]

Here, we demonstrate how rotational coupling between levels emerges naturally in microscopic hierarchical kirigami templates folding in a fluid. We numerically show how the value of this coupling is key to enhance the folding rate and yield, thus defining a metric against which the quality of a kirigami template can be assessed. We rationalize the emergence of an optimal coupling parameter value by mapping our results into a first passage problem.

[a] Department of Chemistry, University College London, 20 Gordon Street, WC1H 0AJ London, UK. E-mail: g.volpe@ucl.ac.uk
[b] Institute of High Performance Computing, A*STAR, Singapore
[c] School of Chemistry, Chemical Engineering and Biotechnology, Nanyang Technological University, 62 Nanyang Drive, 637459, Singapore
[d] Departamento de Física, Faculdade de Ciências, Universidade de Lisboa, 1749-016 Lisboa, Portugal
[e] Centro de Física Teórica e Computacional, Faculdade de Ciências, Universidade de Lisboa, 1749-016 Lisboa, Portugal
[f] Department of Mathematical Sciences, University of Bath, Claverton Down, Bath, BA2 7AY, UK
[g] Department of Mathematics, University College London, Gordon Street, London, WC1H 0AY, UK
[h] Department of Applied Mathematics and Theoretical Physics, University of Cambridge, Centre for Mathematical Sciences, CB3 0WA, UK

† Electronic supplementary information (ESI) available. See DOI: https://doi.org/10.1039/d3sm01474f

Results and discussion

As model target structures, we consider double pyramids with three sets of two hinged lateral faces of constant height h (Fig. 1a and b). The upper level's faces are hinged to the respective lower level's faces, which a second hinge tethers to the substrate. Two target angles define the structures' three-dimensional geometry (Fig. 1a): $\phi_l \in (0,\pi)$ and $\phi_u \in (-\pi,\pi)$, respectively defined with respect to the substrate and the plane containing the lower face. Based on the choice of angles, the target structures span from hourglass shapes to diamonds and their two-dimensional templates (Fig. 1b) are obtained by cutting and unfolding the edges of their lateral faces. Two time-dependent angles, $\theta_l(t)$ and $\theta_u(t)$, describe the motion of the two hinges during the folding process driven in the fluid by thermal fluctuations (here, in water at room temperature).

A model for the coupled motion of two faces joined by a hinge can be derived using the approach of 'resistive-force theory'.[43,44] Under this approach, the hydrodynamic drag on each face combines with constraints of vanishing net torque and force (owing to the absence of inertia) to yield a coupled equation of motion, while secondary hydrodynamic interactions between the faces are neglected:[42]

$$\dot{\theta}_u^i = \hat{\alpha}(\theta_u^i)\dot{\theta}_l^i - \frac{3}{Ch^2}F_u^i, \tag{1a}$$

$$\dot{\theta}_l^i = \hat{\beta}(\theta_u^i)\dot{\theta}_u^i + \frac{6\hat{\beta}(\theta_u^i)}{\cos(\theta_u^i)Ch^2}F_l^i, \tag{1b}$$

where F_l^i and F_u^i are the magnitudes of the forces acting in the normal direction to the lower and upper faces (Fig. 1c and Fig. S1, ESI†), respectively, $C < 0$ is the normal hydrodynamic resistive force coefficient for each face, here assumed equal,[42] and $\hat{\alpha} < 0$ and $\hat{\beta} < 0$ provide negative feedbacks (*i.e.* contrary motions) between the faces.

Eqn (1) shows how the motion of the two hinged faces is thus naturally coupled due to the fluid's hydrodynamic resistance. In fact, for small upper angles θ_u^i, the feedback terms in eqn (1) become roughly constant and are dominated by $\hat{\alpha}$ ($\hat{\alpha} = 15\hat{\beta}$ in this limit). Indeed, $\hat{\alpha}$ remains roughly an order of magnitude larger than $\hat{\beta}$ over a wide range of θ_u^i (Fig. S2, ESI†),[42] *i.e.* the upper face is much more strongly affected by the motion of the lower than the lower is by the upper.

For microscopic structures such as those obtained by folding reconfigurable DNA patterns,[45] the folding can be determined and driven by thermal fluctuations. As discussed previously for one-level structures,[37] the driving forces (F_l^i and F_u^i) change rapidly in similar cases, being well described by stochastic processes uncorrelated in space and time.[46] The variance of this process, and hence the typical rotational diffusion coefficients D_θ for each face, can be derived assuming equipartition.[42] For a hinged circular disc of radius $h/\sqrt{\pi}$, $D_\theta = \frac{3k_BT}{8\mu h^3}$, where k_B is the Boltzmann constant, T the thermostat temperature, and μ the fluid viscosity.[42] For h being $\mathcal{O}$ (μm) to $\mathcal{O}$ (10 μm), D_θ varies from $\mathcal{O}$ (10 rad^2 s^{-1}) to $\mathcal{O}$ (10^{-3} rad^2 s^{-1}).

To primarily explore the role of the dominant lower-to-upper coupling of the faces, and taking thermal fluctuations as the only drive, we consider the reduced model

$$\dot{\theta}_u^i = \alpha\dot{\theta}_l^i + \sqrt{2D_{\theta_u}}\eta_{\theta_u}^i, \tag{2a}$$

$$\dot{\theta}_l^i = \sqrt{2D_{\theta_l}}\eta_{\theta_l}^i, \tag{2b}$$

where D_{θ_l} and D_{θ_u} are the rotational diffusion coefficients of the lower and upper faces, respectively, and $\eta_{\theta_l}^i$ and $\eta_{\theta_u}^i$ are independent white noise processes.[46] Here, the weaker coupling is neglected and the dominant coupling is parameterized by a single dimensionless constant α; a reference value of α is obtained in the limit $\theta_u^i \to 0$, which gives $\alpha_H \equiv \hat{\alpha}(\theta_u^i \to 0) = -5/2$. This follows directly from the model in eqn (1) but, more generally, we leave α as a free parameter to assess the quality of a given kirigami template in terms of the maximum achievable folding rate and yield and to allow for this feedback to be engineered. Indeed, even

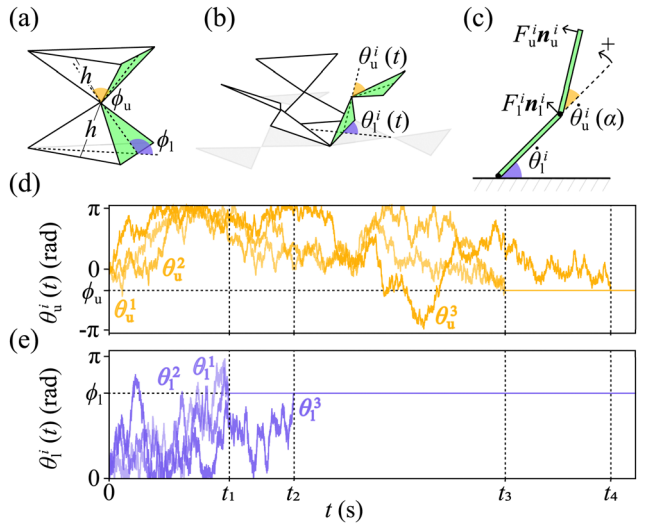

Fig. 1 Folding of a two-level kirigami. (a) Example of two-level kirigami target structure formed by three sets of two hinged flat sheets (faces) of constant height h. Two target angles, ϕ_l and ϕ_u, define the structure's lower and upper levels, respectively. Here, $\phi_l = \frac{2\pi}{3}$rad and $\phi_u = -\frac{\pi}{3}$rad produce an hourglass shape. (b) Two-dimensional template (gray area) for the target structure in (a). The upper faces are hinged to the respective lower ones, which are hinged to the substrate. During folding, the motion of each set of connected faces (i = 1, 2, 3) is described by the angles of the lower and upper levels as a function of time, $\theta_l^i(t)$ and $\theta_u^i(t)$, respectively defined with respect to the substrate and the plane of the lower face. (c) The folding dynamics can be modeled by considering the overdamped motion of each set i of faces ($\dot{\theta}_l^i$ and $\dot{\theta}_u^i$) under driving forces F_l^i and F_u^i (here, thermal noise), respectively acting on the lower and upper level.[42] Both forces are directed along the unitary vectors normal to the faces ($\boldsymbol{n}_l^i$ and $\boldsymbol{n}_u^i$), causing their rotation around the hinges. Counterclockwise rotations of the top level increase the upper angle towards positive values, with $\theta_u^i(t) = 0$ when the upper and lower levels are parallel. Due to the fluid's hydrodynamic resistance, the motion of the upper faces is naturally coupled to that of the respective lower faces with a dimensionless coupling constant $\alpha < 0$ (here, $\alpha = \alpha_H = -5/2$). (d) and (e) Sample trajectories of (d) upper and (e) lower faces. The horizontal dashed lines indicate the target angles ϕ_l and ϕ_u. The vertical dashed lines represent irreversible binding events between two faces of the lower (t_1 and t_2) or upper (t_3 and t_4) levels.

within the modeling framework of eqn (1), it is possible to change the strength of coupling by allowing variability in the properties of the two faces and the hinge between them.[42]

For each set of coupled faces (Fig. 1), we solve these differential equations numerically with an example value of $D_{\theta_l} = D_{\theta_u} = 0.64$ rad^2 s^{-1} (around the middle of the possible D_θ range) using the Euler integration scheme (timestep $\Delta\tau = 10$ μs).[46] We however note that our observations are qualitatively independent of the value of D_θ (Fig. S3, ESI†). We model the substrate as reflective boundary[46] and detect and correct face collisions with the Gilbert–Johnson–Keerthi algorithm.[47] We fix a cutoff time $\tau_{cut} = 2 \times 10^8 \Delta\tau$, when we consider misfolded any structure which is not folded completely. Fig. 1d and e shows sample trajectories for the faces of the upper and lower levels when $\alpha = \alpha_H$, highlighting how the system converges to the target structure through a series of four binding events between faces of the lower level first followed by the upper level. Each event is defined by two faces being at their target angle ($\pm\pi/180$) concomitantly. We consider these events irreversible as in experiments with micro-polyhedra[25] and DNA origami.[39]

Fig. 2 shows that varying the coupling by tuning the value – and sign – of the coupling parameter α can optimize the folding process. To avoid bias from long folding events, we define the folding rate, k_α, as a function of α by taking the reciprocal of the folding time of each event before calculating the average for all successfully folded structures. The contribution of folding events that fold in a time $t > \tau_{cut}$ to the overall folding rate is therefore near zero and does not influence the numerical results significantly. Fig. 2a shows that, for the structure in Fig. 1 with an obtuse ϕ_l and a negative ϕ_u, the folding rate at negative α ($\alpha = -1$) is enhanced by ≈1.3 and ≈1.1 times when compared to no coupling ($\alpha = 0$) and the rate at α_H. For the diamond with an acute ϕ_l and a positive ϕ_u instead (Fig. 2b), positive α values can enhance folding by up to ≈6 and ≈4.5 times when compared to the rates at α_H and for no coupling, respectively. As mentioned earlier, these observations are qualitatively independent of the value of D_θ (Fig. S3, ESI†). Interestingly, for both structures, the α values that optimize the rate (α_{opt}) and the yield (the percentage of fully folded structures within τ_{cut}) are closely related, with yields of ≈70% and ≈61% at α_{opt} (against the highest yields of ≈74% and ≈62%) in Fig. 2a and b, respectively. A broad range of negative α values below $\alpha = -1$ can be obtained in practice by modifying the relative lengths of the upper and lower faces in the kirigami template.[42] Although this limits the experimentally attainable α values, our results allow one to assess the quality of a given kirigami design against its maximum attainable yield and folding rates as a function of the dominant coupling parameter α.

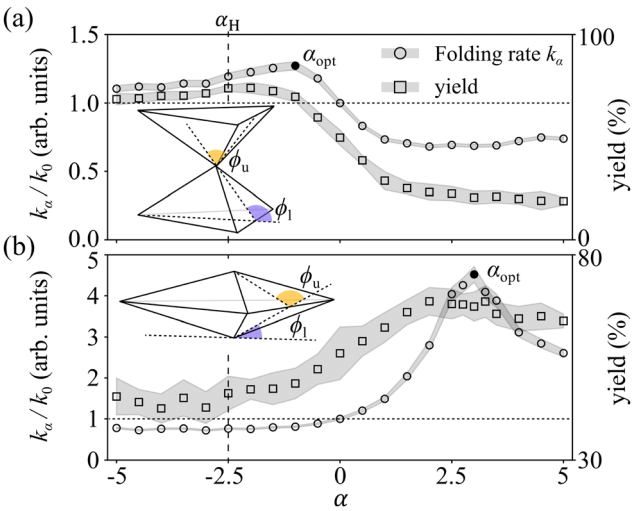

Fig. 2 Folding dependence on the coupling parameter. (a) and (b) Folding rate k_α (circles) and yield (squares) as a function of coupling parameter α for two exemplary kirigami structures: (a) an hourglass (as in Fig. 1) and (b) a diamond ($\phi_l = 0.61$ rad, $\phi_u = 1.92$ rad). The rate is obtained by taking the reciprocal of the folding times of individual events then calculating the average across all successfully folded structures. Depending on the target geometry, (a) negative or (b) positive values of α can lead to optimal folding (α_{opt}, filled circles). The vertical dashed lines show α_H for reference. Folding rates are normalized to k_0 (k_α for $\alpha = 0$). The shaded areas represent one standard error from 5000 folding events lasting up to the cutoff time τ_{cut}.

Fig. 2 suggests that the value of the coupling between faces can optimize both folding rate and yield of a given kirigami structure at once. This observation can be generalized to a variety of structures (examples in Fig. 3a) with varying target angles ϕ_l and ϕ_u (Fig. 3 and Fig. S4, ESI†). To a first analysis, the value of ϕ_u is the decisive factor discerning whether a negative (for $\phi_u < 0$) or positive α (for $\phi_u > 0$) optimizes the folding rate (Fig. 3b). Structures with upper levels opening away from the center (*e.g.* Fig. 3bII, IV and VI) tend to benefit from a negative coupling to their respective lower levels, while structures whose upper levels point towards their centers (*e.g.* Fig. 3bI) tend to fold faster with a positive coupling. The absence of coupling instead tends to be optimal for structures (*e.g.* Fig. 3bIII and Fig. S4a, ESI†) where the lower and upper levels roughly lie on the same plane ($\phi_u \approx 0$). Indeed, the benefits in folding rate because of coupling between levels increases the farther a structure is from this condition, as $k_\alpha \approx k_0$ around $\phi_u \approx 0$ (Fig. 3c). These results further highlight the importance of choosing a kirigami template based on the optimal value of the coupling parameter, as the folding of target structures in the ranges of relatively smaller upper angles and positive upper angles tends to be comparatively inhibited by the sub-optimal coupling due to the natural hydrodynamic resistance of the hinged faces.[42] The range of ϕ_u values where no coupling is advantageous broadens asymmetrically towards positive α values as ϕ_l increases towards π. In these situations, stronger coupling tends to push the upper level's faces against the substrate, thus delaying the convergence to the target structure. As in Fig. 2, the value of α that optimizes folding rate also roughly optimizes yield (Fig. S4b–d, ESI†), thus enabling one to assess the quality of a kirigami template in terms of these two quantities: for most structures, the ratio between the yield achieved at α_{opt} and the maximum yield at any α (max(yield), Fig. S4b, ESI†) is close to one (Fig. S4c, ESI†), and the distance between these two α values is often close to zero ($|\alpha_{max(yield)} - \alpha_{opt}| \approx 0$, Fig. S4d, ESI†). Larger separations between these two values are possible but often coincide with regions where the

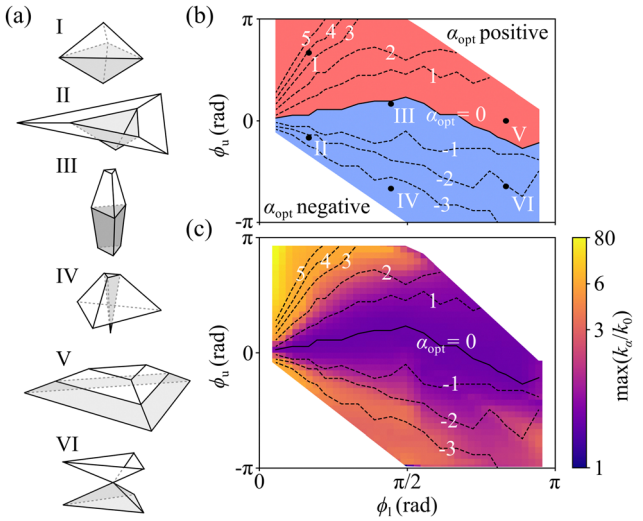

Fig. 3 Optimal coupling for different target structures. (a) Examples of different kirigami target structures with varying target angles ϕ_l and ϕ_u (Fig. 1a). As ϕ_l increases from acute to obtuse, the lower levels (gray faces) transition from inverted pyramids (I, II and IV) as in Fig. 2b to regular pyramids (VI) as in Fig. 2a *via* truncated pyramids (III and V). For ϕ_u going from negative to positive values, the upper level goes from an umbrella shape, either convex (IV) or concave (VI), to a pyramid (I, III and V), truncated or not, through a flat plane (II). (b) Phase diagram of the optimal coupling parameter α_{opt} for different structures: either a negative (blue) or positive (red) α is optimal (Fig. S4a, ESI†). (c) Highest folding rate max(k_z) at any α for different structures. Folding rates are normalized to k_0. In (b) and (c), the black isolines highlight structures whose folding is optimal at (dashed) a given α or (solid) in the absence of coupling (α = 0). Each data point is an average of 5000 folding events.

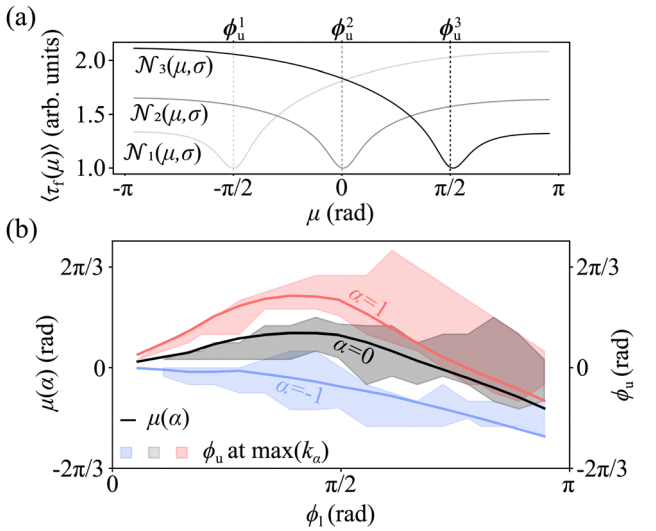

Fig. 4 Assessing optimal coupling as a first passage problem. (a) Expected mean first passage time $\langle\tau_f(\mu)\rangle$ of two upper level's faces to a target angle ϕ_u^n (with n = 1, 2, 3) at the closing time of the lower level t_2 as a function of the mean μ of the probability distribution of the faces' starting position.[42] Here, the starting positions of each face are drawn from a one-dimensional Gaussian distribution $\mathcal{N}_n(\mu,\sigma)$ with varying mean μ, fixed variance σ and reflected at the boundaries of the possible range of angles.[42] Three cases are shown: $\phi_u^1 = -\frac{\pi}{2}$, $\phi_u^2 = 0$ and $\phi_u^3 = \frac{\pi}{2}$. The minimum value of $\langle\tau_f(\mu)\rangle$ occurs when $\mu \approx \phi_u^n$. (b) For a given α and lower level's target angle ϕ_l (see also Fig. S6, ESI†), the means of the probability distributions of the angles θ_u^l of the upper level's faces when the lower level has closed (solid lines) are well captured by the range of possible structures with the highest folding rate at that α value (Fig. 3c) once the numerical uncertainty in determining the position of max(k_z) is accounted for (shaded areas). This uncertainty is calculated taking the largest between the discretization step in α and the range of data points around the peak falling within the standard error.

yield is relatively insensitive to the exact α value (Fig. S4c, ESI†) or where advantages over no coupling are negligible (Fig. 3c).

To rationalize the emergence of an optimal coupling parameter α, we can map our results into a first passage problem to a target.[42] This choice is justified as, for single-level pyramids with less than five faces, the folding time is dominated by the closing of the first pair of faces – event well described as a first passage problem in a two-dimensional random walk.[37] Thus, the total folding time for single-level structures depends on the initial location of its faces.[37] Similarly, for two-level structures, when the lower level folds much faster than the upper as observed here in simulations, the closing of the first pair of upper level's faces after the lower level has closed completely is the event dominating the folding of most structures. The optimal value of α should then be the one that leads to the distribution of angles in the upper level when the lower level has closed that minimizes the time for the first two faces of the upper level to reach their target angle ϕ_u. Starting from a location drawn from a one-dimensional Gaussian distribution $\mathcal{N}(\mu,\sigma)$ with varying mean $\mu(\alpha)$ and fixed variance σ and reflected at the boundaries to ensure its proper normalization,[42] the mean first passage time to a trap at location $\boldsymbol{\phi} = (\phi_u, \phi_u)$ of a two-dimensional random walk on a lattice with reflective boundaries is calculated as[48]

$$\langle\tau_f(\mu)\rangle = \iint T_{\boldsymbol{\theta}_0\to\boldsymbol{\phi}} P(\boldsymbol{\theta}_0) \mathrm{d}\boldsymbol{\theta}_0, \quad (3)$$

where $T_{\boldsymbol{\theta}_0\to\boldsymbol{\phi}}$ is the first passage time to the trap starting from position $\boldsymbol{\theta}_0 = (\theta_{01},\theta_{02})$ on the lattice with probability $P(\boldsymbol{\theta}_0) = \mathcal{N}(\mu,\sigma)_{|\theta_{01}}\,\mathcal{N}(\mu,\sigma)_{|\theta_{02}}$.[42] Fig. 4a shows that $\langle\tau_f(\mu)\rangle$ should be minimized when α is chosen so that $\mu(\alpha) \approx \phi_u$. Our numerical results confirm that, for a given α, the means of the distributions of the angles in the upper level after to lower has closed completely (exemplary distributions in Fig. S5, ESI†) as a function of the lower level target angle ϕ_l closely resemble the upper level target angles ϕ_u of the structures with the highest folding rate at that α (Fig. 4b and Fig. S6, ESI†). This observation provides an effective rule to assess the quality of a kirigami template to achieve a target geometry against its maximum attainable yield and folding rate as a function of the experimentally possible values of the coupling parameter α.[42]

Conclusions

In conclusion, we have shown how the folding of microscopic hierarchical two-level kirigami structures in a fluid develops a natural degree of coupling between levels due to hydrodynamic resistance. This coupling is essential to understand the folding dynamics of similar structures as both folding rate and yield are

impacted in its absence. Moreover, we show how rational design rules (*e.g.* based on solving a first passage time problem) can explain the emergence of an optimal coupling parameter for maximizing folding rates and yield as a function of the target geometry. Even within the reduced modeling framework of eqn (1), the coupling parameter α allows optimization of the folding process (in terms of folding rate and yield) in a broad range of negative values below $\alpha = -1$ by tuning the relative lengths of the lower and upper faces in the kirigami template. Outside of the experimentally attainable α values, our results can be employed to assess and select optimal designs for a given three-dimensional target structure from a set of different two-dimensional templates based on the efficiency of the folding pathway against the maximum attainable folding rate and yield. Additionally, in these cases, further degrees of control could be introduced to optimize the folding pathway by, *e.g.*, engineering the hydrodynamic resistance of the faces or exploiting active or driven hinges.[42] We envisage that similar design rules could be adopted to engineer fast self-folding hierarchical multi-level kirigami structures for applications in, *e.g.*, soft robotics, mechanical actuators and metamaterials.[9,10,13–20]

Author contributions

Author contributions based on CRediT. Conceptualization: NAMA, GV. Data curation: MPB, NAMA, BJW, DRH, GV. Formal analysis: MPB, NAMA, BJW, DRH, GV. Funding acquisition: QXP, RN, GV. Investigation: MPB, NAMA, BJW, DRH, GV. Methodology: MPB, NAMA, BJW, DRH, GV. Project administration: QXP, RN, GV. Resources: QXP, RN, GV. Software: MPB. Supervision: NAMA, QXP, RN, GV. Validation: MPB, NAMA, GV. Visualization: MPB, BJW. Writing – original draft: MPB, NAMA, BJW, DRH, GV. Writing – review and editing: MPB, NAMA, BJW, DRH, QXP, RN, GV.

Conflicts of interest

There are no conflicts to declare.

Acknowledgements

MPB, QXP and GV are grateful to the studentship funded by the A*STAR-UCL Research Attachment Programme through the EPSRC M3S CDT (EP/L015862/1). NAMA acknowledges financial support from the Portuguese Foundation for Science and Technology (FCT) under the contracts no. UIDB/00618/2020 and UIDP/00618/2020. BJW is supported by the Royal Commission for the Exhibition of 1851. NAMA and GV acknowledge support from the UCL MAPS Faculty Visiting Fellowship programme.

Notes and references

1 X. Ning, X. Wang, Y. Zhang, X. Yu, D. Choi, N. Zheng, D. S. Kim, Y. Huang, Y. Zhang and J. A. Rogers, *Adv. Mater. Interfaces*, 2018, **5**, 1800284.
2 X. Cheng and Y. Zhang, *Adv. Mater.*, 2019, **31**, e1901895.
3 S. Chen, J. Chen, X. Zhang, Z.-Y. Li, J. Li and J. Li, *Light: Sci. Appl.*, 2020, **9**, 75.
4 K. Kuribayashi-Shigetomi, H. Onoe and S. Takeuchi, *PLoS One*, 2012, **7**, e51085.
5 R. Fernandes and D. H. Gracias, *Adv. Drug Delivery Rev.*, 2012, **64**, 1579–1589.
6 W. Guo, M. Li and J. Zhou, *Smart Mater. Struct.*, 2013, **22**, 115028.
7 H. Fu, K. Nan, W. Bai, W. Huang, K. Bai, L. Lu, C. Zhou, Y. Liu, F. Liu, J. Wang, M. Han, Z. Yan, H. Luan, Y. Zhang, Y. Zhang, J. Zhao, X. Cheng, M. Li, J. W. Lee, Y. Liu, D. Fang, X. Li, Y. Huang, Y. Zhang and J. A. Rogers, *Nat. Mater.*, 2018, **17**, 268–276.
8 J. D. Paulsen, *Annu. Rev. Condens. Matter Phys.*, 2019, **10**, 431–450.
9 K. Malachowski, M. Jamal, Q. Jin, B. Polat, C. J. Morris and D. H. Gracias, *Nano Lett.*, 2014, **14**, 4164–4170.
10 R. Niu, C. X. Du, E. Esposito, J. Ng, M. P. Brenner, P. L. McEuen and I. Cohen, *Proc. Natl. Acad. Sci. U. S. A.*, 2019, **116**, 24402–24407.
11 R. M. Erb, J. S. Sander, R. Grisch and A. R. Studart, *Nat. Commun.*, 2013, **4**, 1712.
12 T. C. Shyu, P. F. Damasceno, P. M. Dodd, A. Lamoureux, L. Xu, M. Shlian, M. Shtein, S. C. Glotzer and N. A. Kotov, *Nat. Mater.*, 2015, **14**, 785.
13 K. Bertoldi, V. Vitelli, J. Christensen and M. Van Hecke, *Nat. Rev. Mater.*, 2017, **2**, 17066.
14 H. Fang, S. A. Chu, Y. Xia and K. Wang, *Adv. Mater.*, 2018, **30**, e1706311.
15 H. Zhang and J. Paik, *Adv. Functional Mater.*, 2022, **32**, 2107401.
16 C. Wang, C. Wang, Z. Huang and S. Xu, *Adv. Mater.*, 2018, **30**, e1801368.
17 D. Rus and M. T. Tolley, *Nat. Rev. Mater.*, 2018, **3**, 101–112.
18 M. Z. Miskin, A. J. Cortese, K. Dorsey, E. P. Esposito, M. F. Reynolds, Q. Liu, M. Cao, D. A. Muller, P. L. McEuen and I. Cohen, *Nature*, 2020, **584**, 557–561.
19 A. Bacchetti, P. Lloyd, S. Taccola, E. Fakhoury, S. Cochran, R. A. Harris, P. Valdastri and J. H. Chandler, *Front. Robot. AI*, 2022, **9**, 1040984.
20 Y. Dong, L. Wang, N. Xia, Z. Yang, C. Zhang, C. Pan, D. Jin, J. Zhang, C. Majidi and L. Zhang, *Sci. Adv.*, 2022, **8**, eabn8932.
21 M. Stern, V. Jayaram and A. Murugan, *Nat. Commun.*, 2018, **9**, 4303.
22 N. Araújo, R. Da Costa, S. Dorogovtsev and J. Mendes, *Phys. Rev. Lett.*, 2018, **120**, 188001.
23 C. D. Santangelo, *Soft Matter*, 2020, **16**, 94–101.
24 Y.-K. Lee, Z. Xi, Y.-J. Lee, Y.-H. Kim, Y. Hao, H. Choi, M.-G. Lee, Y.-C. Joo, C. Kim, J.-M. Lien and I.-S. Choi, *Sci. Adv.*, 2020, **6**, eaax6212.
25 S. Pandey, M. Ewing, A. Kunas, N. Nguyen, D. H. Gracias and G. Menon, *Proc. Natl. Acad. Sci. U. S. A.*, 2011, **108**, 19885–19890.
26 T. Castle, Y. Cho, X. Gong, E. Jung, D. M. Sussman, S. Yang and R. D. Kamien, *Phys. Rev. Lett.*, 2014, **113**, 245502.
27 L. H. Dudte, E. Vouga, T. Tachi and L. Mahadevan, *Nat. Mater.*, 2016, **15**, 583–588.

28 P. Dieleman, N. Vasmel, S. Waitukaitis and M. van Hecke, *Nat. Phys.*, 2020, **16**, 63–68.
29 C. D. Santangelo, *Annu. Rev. Condens. Matter Phys.*, 2017, **8**, 165–183.
30 Y. Zhang, Z. Yan, K. Nan, D. Xiao, Y. Liu, H. Luan, H. Fu, X. Wang, Q. Yang, J. Wang, W. Ren, H. Si, F. Liu, L. Yang, H. Li, J. Wang, X. Guo, H. Luo, L. Wang, Y. Huang and J. A. Rogers, *Proc. Natl. Acad. Sci. U. S. A.*, 2015, **112**, 11757–11764.
31 G. P. T. Choi, L. H. Dudte and L. Mahadevan, *Phys. Rev. Res.*, 2021, **3**, 043030.
32 K. Xiao, Z. Liang, B. Zou, X. Zhou and J. Ju, *Nat. Commun.*, 2022, **13**, 7474.
33 P. W. K. Rothemund, *Nature*, 2006, **440**, 297–302.
34 T. G. Leong, P. A. Lester, T. L. Koh, E. K. Call and D. H. Gracias, *Langmuir*, 2007, **23**, 8747–8751.
35 A. Azam, K. E. Laflin, M. Jamal, R. Fernandes and D. H. Gracias, *Biomed. Microdevices*, 2011, **13**, 51–58.
36 P. M. Dodd, P. F. Damasceno and S. C. Glotzer, *Proc. Natl. Acad. Sci. U. S. A.*, 2018, **115**, E6690–E6696.
37 H. Melo, C. Dias and N. Araújo, *Commun. Phys.*, 2020, **3**, 154.
38 T. S. A. N. Simões, H. P. M. Melo and N. A. M. Araújo, *Eur. Phys. J. E: Soft Matter Biol. Phys.*, 2021, **44**, 46.
39 F. Hong, F. Zhang, Y. Liu and H. Yan, *Chem. Rev.*, 2017, **117**, 12584–12640.
40 A. Azam, T. G. Leong, A. M. Zarafshar and D. H. Gracias, *PLoS One*, 2009, **4**, e4451.
41 N. Bao, Q. Liu, M. F. Reynolds, M. Figueras, E. Smith, W. Wang, M. C. Cao, D. A. Muller, M. Mavrikakis, I. Cohen, P. L. McEuen and N. L. Abbott, *Proc. Natl. Acad. Sci. U. S. A.*, 2023, **120**, e2221740120.
42 ESI†.
43 G. J. Hancock, *Proc. R. Soc. A*, 1953, **217**, 96–121.
44 J. Gray and G. J. Hancock, *J. Exp. Biol.*, 1955, **32**, 802–814.
45 M. Kim, C. Lee, K. Jeon, J. Y. Lee, Y.-J. Kim, J. G. Lee, H. Kim, M. Cho and D.-N. Kim, *Nature*, 2023, **619**, 78–86.
46 G. Volpe and G. Volpe, *Am. J. Phys.*, 2013, **81**, 224–230.
47 E. Gilbert, D. Johnson and S. Keerthi, *IEEE J. Robot. Autom.*, 1988, **4**, 193–203.
48 L. Giuggioli, *Phys. Rev. X*, 2020, **10**, 021045.

